



Atomic-engineered gradient tunable solid-state metamaterials

Zhiyuan Yan^a, Albertus Denny Handoko^b, Weikang Wu^c, Chuchu Yang^d, Hao Wang^e, Meltem Yilmaz^{b,f}, Zhiyong Zhang^g, Libo Cheng^h, Xinbin Chengⁱ, Ghim Wei Ho^a , Bin Feng^d, Naoya Shibata^d, Rong Zhao^j, Joel K. W. Yang^e, Chong Tow Chong^e, Yuichi Ikuhara^d , and Cheng-Wei Qiu^{a,k,1}

Affiliations are included on p. 8.

Edited by David Weitz, Harvard University, Cambridge, MA; received May 9, 2024; accepted August 21, 2024

Metamaterial has been captivated a popular notion, offering photonic functionalities beyond the capabilities of natural materials. Its desirable functionality primarily relies on well-controlled conditions such as structural resonance, dispersion, geometry, filling fraction, external actuation, etc. However, its fundamental building blocks—meta-atoms—still rely on naturally occurring substances. Here, we propose and validate the concept of gradient and reversible atomic-engineered metamaterials (GRAM), which represents a platform for continuously tunable solid metaphotonics by atomic manipulation. GRAM consists of an atomic heterogeneous interface of amorphous host and noble metals at the bottom, and the top interface was designed to facilitate the reversible movement of foreign atoms. Continuous and reversible changes in GRAM's refractive index and atomic structures are observed in the presence of a thermal field. We achieve multiple optical states of GRAM at varying temperature and time and demonstrate GRAM-based tunable nanophotonic devices in the visible spectrum. Further, high-efficiency and programmable laser raster-scanning patterns can be locally controlled by adjusting power and speed, without any mask-assisted or complex nanofabrication. Our approach casts a distinct, multilevel, and reversible postfabrication recipe to modify a solid material's properties at the atomic scale, opening avenues for optical materials engineering, information storage, display, and encryption, as well as advanced thermal optics and photonics.

atomic manipulation | phase transition | heterogeneous interface | metaoptics

Metaphotonics, a captivating field, promises photonic functionalities that can engineer electromagnetic waves in metamaterials to produce unusual physical phenomena (1–3). It holds potential applications in various fields such as display, sensor, information communication, robotics, encryption, and stealth technologies (4, 5). However, most metamaterials are passive, with properties fixed once fabricated, limiting the exotic advantages of passive metaphotonics over its natural counterparts (6–8). Active metamaterials introduce a new dimension to the field with promising applications in display, imaging, computing, light detection, and range, optical camouflage, nonreciprocal-photonics and more (9–12). Current tunable metaphotonics rely on either soft materials or active solid materials. While soft-based tunable metaphotonics have been achieved through mechanical stimulus (13–17), integrating them with the top-down nanofabrication process for current semiconductors remains a challenge. Solid-state metadevices have garnered significant attention due to their compatibility with existing semiconductor processes. To create active metamaterials that can dynamically change their properties or structures, one of the main approaches is to use materials that can alter their refractive index in response to external stimuli, such as phase change materials (18–21) and chemical reactions (22, 23). These materials' index can be switched between two different and reversible states, enabling tunable functionalities between two boundary states. However, these mechanisms typically allow only two distinct states of tunability (as illustrated in Fig. 1A). Challenges remain in achieving multilevel programmability at the subnanoscale and integrating with existing solid-state foundry processes (7). Therefore, there is a need for new methods to manipulate solid materials at the atomic scale, which would enhance the development of functional nanoscale and subnanoscale devices and high-density chip design.

The concept of atomic manipulation has been a pivotal aim in the realms of science and engineering, drawing inspiration from Feynman's seminal 1959 lecture (24) and propelled by advancements in both top-down and bottom-up methodologies. This technique allows for the customization of materials' chemical and physical attributes across various scales and has found extensive application in both core interdisciplinary research and the fabrication of practical devices across numerous fields (25–28). Here, we introduce the gradient and reversible atomic-engineered metamaterials (GRAM) method to adjust the composition and structure of materials, enhancing the tunability of material properties

Significance

The gradient and reversible atomic-engineered metamaterials (GRAM) method offers a distinct approach to active metamaterials through precise atomic-manipulation, essential for enhancing multilevel programmability. GRAM leverages phase transitions to control the arrangement of foreign atoms within the host material, enabling continuous, multitiered transformations at the atomic scale. Consequently, solid metamaterials achieve nonbinary tunability with reversible modulation of multiple optical states. This method's adaptability in postsynthesis modifications addresses existing challenges in tuning mechanisms for solid metaoptics. By dynamically controlling noble metal atoms through thermal modulation, GRAM enables flexibility in altering the refractive index and device structures. This adaptability has potential applications in imaging, computing, and optical camouflage, providing a versatile strategy for enhancing performance and overcoming limitations in current solid material tuning techniques.

The authors declare no competing interest.

This article is a PNAS Direct Submission.

Copyright © 2024 the Author(s). Published by PNAS. This article is distributed under [Creative Commons Attribution-NonCommercial-NoDerivatives License 4.0 \(CC BY-NC-ND\)](https://creativecommons.org/licenses/by-nc-nd/4.0/).

¹To whom correspondence may be addressed. Email: chengwei.qiu@nus.edu.sg.

This article contains supporting information online at <https://www.pnas.org/lookup/suppl/doi:10.1073/pnas.2408974121/-/DCSupplemental>.

Published September 18, 2024.

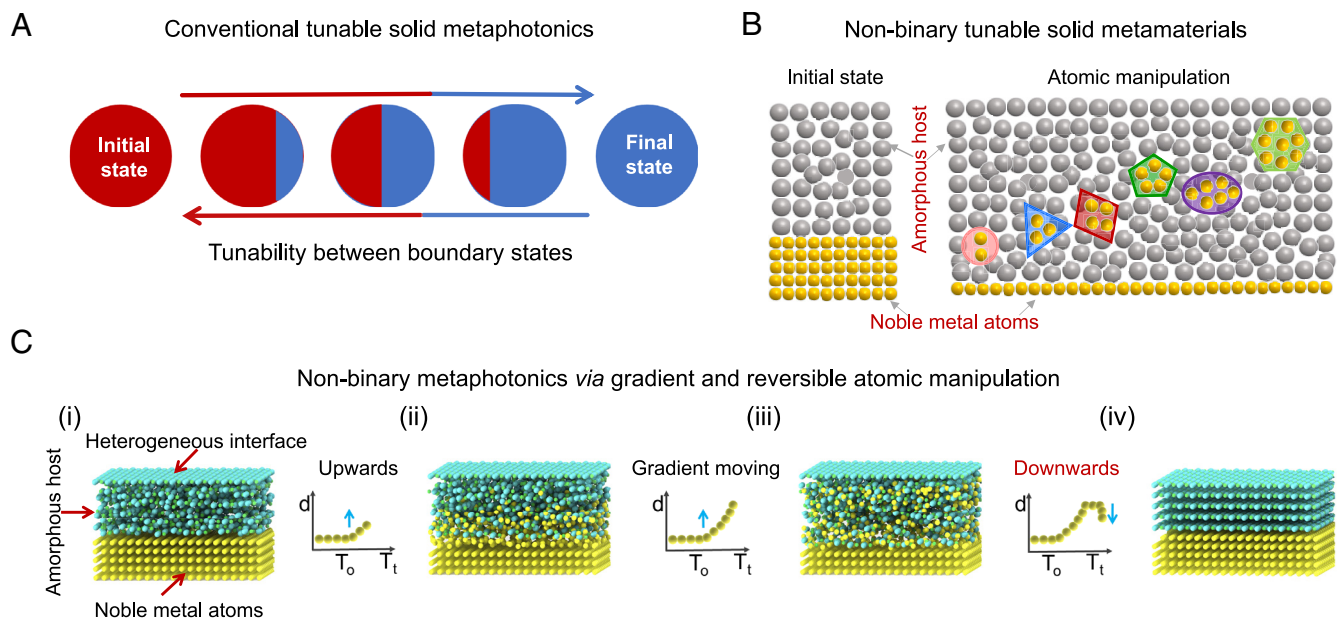


Fig. 1. GRAM concept and atomic manipulation strategy. (A and B) A schematic comparison highlights the limitations of conventional methods (limited tunability) versus the versatility of our approach. Dynamic refractive index changes are represented by colors, while volume alterations are depicted by shape variations. (C) The working principle of gradient and reversible atomic manipulation is demonstrated: the amorphous host with a heterogeneous interface (i) Gradient movement in amorphous host (ii and iii) “Backhaul of metal atoms” during phase transition from amorphous to crystal in the host (iv). *Inset* figures reveal the displacement of noble metal atoms under a thermal field, characterized by the initial temperature (T_0) and real-time temperature (T_t).

postsynthesis and in device structures. Through atomic manipulation, chemical bonds are selectively broken and reformed, altering the material’s composition and, consequently, its structure and refractive index. This process enables a continuous, multitiered, and adaptable transformation of nonbinary tunable solid metamaterials (Fig. 1B). The operational principle is depicted in Fig. 1C, where noble metal atoms are dynamically controlled within a thermal field by modulating temperature and duration. Notably, these atoms gradually integrate into the host material and can revert to their original positions, aided by a top atom heterogeneous interface (i to iv). Unlike previous methods, our GRAM framework affords dynamic and reversible modulation of material properties through the manipulation of picometer-scale movements within the metamaterial’s structural elements, heralding frontiers in photonics applications.

Results and Discussion

Manipulation of Noble Metal Atoms in Amorphous Solids. The development of multitiered nonbinary metamaterials is predicated on the activation of noble metal atoms migrating through a gradient within amorphous semiconductor metal oxides. These noble metals are capable of altering the refractive index and the structural composition by their ingress and egress from the host material. Prior research has delved into the transient movement of metals within crystalline hosts and the genesis of nanofilaments under electric fields, resulting in a static/immobilized interface between the metal and the crystal (29–31), as depicted in Fig. 2A. Nonetheless, achieving a gradient and reversible manipulation of metal atoms within an amorphous host has been challenging due to intense dopant–host interactions and the enduring entrapment of impurities within the host structure (32–35), as shown in Fig. 2B. We designed a top heterogeneous interface that acts as an effective mechanism to reset foreign atoms within the host structure, allowing most to be expelled and revert to their original state. We have ascertained that the gradient movement of noble atoms can be precisely governed by modulating the annealing

temperature and time, and either of the host or the movement of noble metal atoms is volatile (Fig. 2C). Moreover, we have demonstrated that this GRAM methodology can serve as a unique tunable nanophotonic technique, with experimental evidence of its uniform multilevel tunability across a large (10 cm^2) device within the visible spectrum.

In our GRAM device design, we’ve engineered a heterogeneous interface using amorphous Fe_2O_3 paired with a thin layer of crystalline Fe_2O_3 (c- Fe_2O_3). The c- Fe_2O_3 layer serves as a heterogeneous interface, guiding the crystallization of amorphous Fe_2O_3 and the movement of silver (Ag) atoms. Ag was chosen for its notable characteristics such as high mobility, electrical conductivity, antimicrobial properties, and optical advantages, making it suitable for a wide range of applications. Prior research has shown that Ag^+ ions can be transported across various materials when subjected to an electric field, a phenomenon utilized in fields like neuromorphic computing, optoelectronics, and battery technology (36–38). Despite this, devices based on electrochemical metallization often suffer from instability due to unpredictable ion movement, leading to issues like ion trapping and subsequent pathway blockages, which degrade the device’s reversibility and uniformity of switching, particularly in large array configurations (32).

The GRAM methodology we propose ensures stable and consistent multilevel adjustment of extensive solid-state devices through the gradient control of foreign atoms and the attainment of a saturation point of noble metal atoms within the host, facilitated by thermal processes postmanufacture. The operational principle is depicted in Fig. 1C. To validate this approach, we analyzed the microstructure of the GRAM device at various stages of Ag atom migration. Initially, the device underwent a 1-min annealing at $200\text{ }^\circ\text{C}$ (Fig. 2D), and the distinct boundary between Ag and amorphous Fe_2O_3 in the as-deposited GRAM device is visible in *SI Appendix, Fig. S1*. Fig. 2E and F illustrate the energy-dispersive X-ray spectroscopy (EDX) mapping and line profile data for three crucial elements (Fe, Ag, and O) in the GRAM device’s partially altered layer. These data reveal an upward migration of Ag atoms into the amorphous Fe_2O_3 host, following

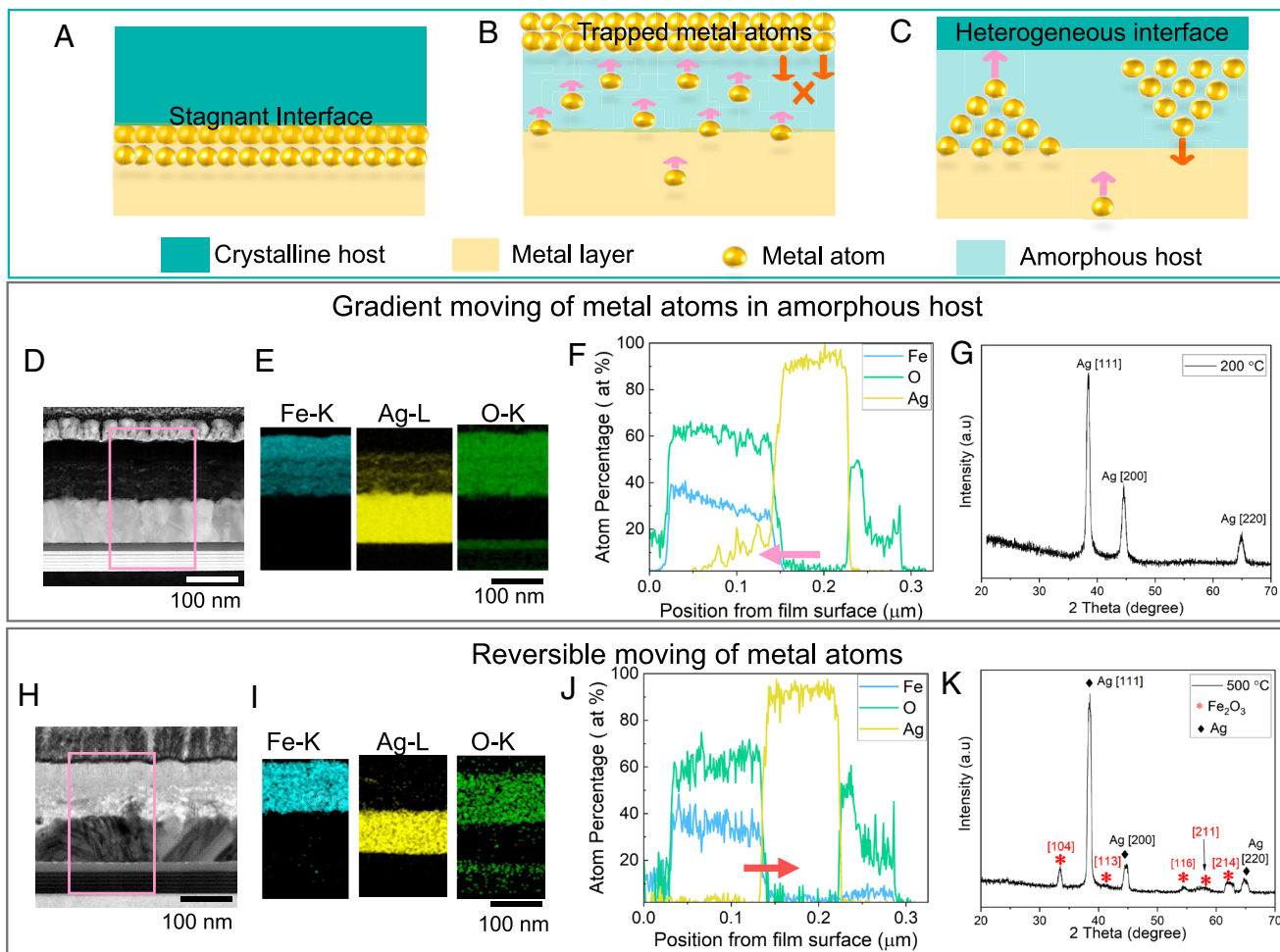


Fig. 2. GRAM powered through the heterogeneous interface and mechanism of the nonbinary metamaterials. (A–C) Schematic illustrations of the differences among the current mechanism of volatile atomic mobility in crystals (A) unidirectional nonvolatile atomic mobility in amorphous host (B) and our proposed GRAM (C): (A) Crystalline host/metal with stagnant interface; (B) amorphous host/metal with metal trapping and overflow; (C) amorphous host with top heterogeneous interface enabling controllable gradient and reversible metal atoms movement. (D–G) Experimental characterization showing gradient moving of noble metal atoms in amorphous host: (D) TEM images displaying the vertical architecture of the metaphotonic device on Si substrate after annealing at 200 °C for 1 min. (E and F) EDX mapping and line profile of three key elements (Fe, Ag, and O). (Scale bar: 100 nm.) (G) XRD results showing the amorphous states of host annealing at 200 °C. (H–K) Experimental characterization showing reversible moving of noble metal atoms assisted by phase transition of host: (H) TEM images of the vertical architecture of the same device annealed at 500 °C for 1 min. (I and J) EDX mapping and line profile of three key elements (Fe, Ag, and O). (Scale bar: 100 nm.) (K) XRD characterization showing the crystalline state of host after annealing at 500 °C.

a gradient pattern. Postannealing, the high-resolution transmission electron microscopy imagery confirms the amorphous state of amorphous Fe_2O_3 , and the selected area electron diffraction (SAED) pattern (*SI Appendix, Fig. S2*) along with X-ray diffraction (XRD) analysis (Fig. 2I) exhibit the amorphous regions within the amorphous Fe_2O_3 , indicating long-range disorder. It's noteworthy that the modified condition stabilizes after annealing, suggesting that the process can be finely calibrated or monitored in situ to achieve specific properties. Comprehensive elemental mapping of GRAM devices annealed at 200 °C and 500 °C is available in *SI Appendix, Fig. S3*, with full elemental line profiles in *SI Appendix, Fig. S4*, and detailed XRD analyses at 200 °C and 500 °C in *SI Appendix, Fig. S5*.

The reversible manipulation of noble metal atoms is facilitated by the phase change in the amorphous host (The schematic process in *Movie S1*). This was demonstrated by annealing a GRAM device at 500 °C for 1 min, as shown in Fig. 2H. The resulting EDX mapping and line profiles, detailed in Fig. 2I and J, reveal negligible Ag signals presence within the amorphous Fe_2O_3 host. The SAED pattern, further detailed in *SI Appendix, Fig. S2*, displays well-defined crystal planes characteristic of polycrystalline host. XRD analyses, as seen in *SI Appendix, Fig. S5*, corroborate

these findings, confirming the host's phase transition as illustrated in Fig. 2G and K. By varying the annealing temperatures, we can precisely control and reverse the movement of Ag atoms within the amorphous host, allowing them to return to their original state postcrystallization, thus proving the controllability and reversibility of noble metal atom manipulation in GRAM devices.

Phase Transformation Enabling the Reversible Atom Movement.

The innovative atom heterogeneous interface facilitates a low phase transition threshold in solid materials, allowing noble metal atoms to be reversibly displaced and then restored to their original states during the host's phase transition, as illustrated in Fig. 2C. A pivotal inquiry arises regarding the mechanism that permits metal atoms to revert to their initial positions rather than becoming permanently embedded in the host. To elucidate this seemingly paradoxical reversible movement of metal atoms, molecular dynamics (MD) simulations were conducted. These simulations modeled the heterogeneous interface to monitor the phase transition from top to bottom, capturing both the initial state and the annealed state at 800 K (Fig. 3A–D). *Movie S2* displays the whole simulation process. The simulations reveal that the ultrathin crystalline heterogeneous interface initiates a

MD simulations: phase transition of amorphous host

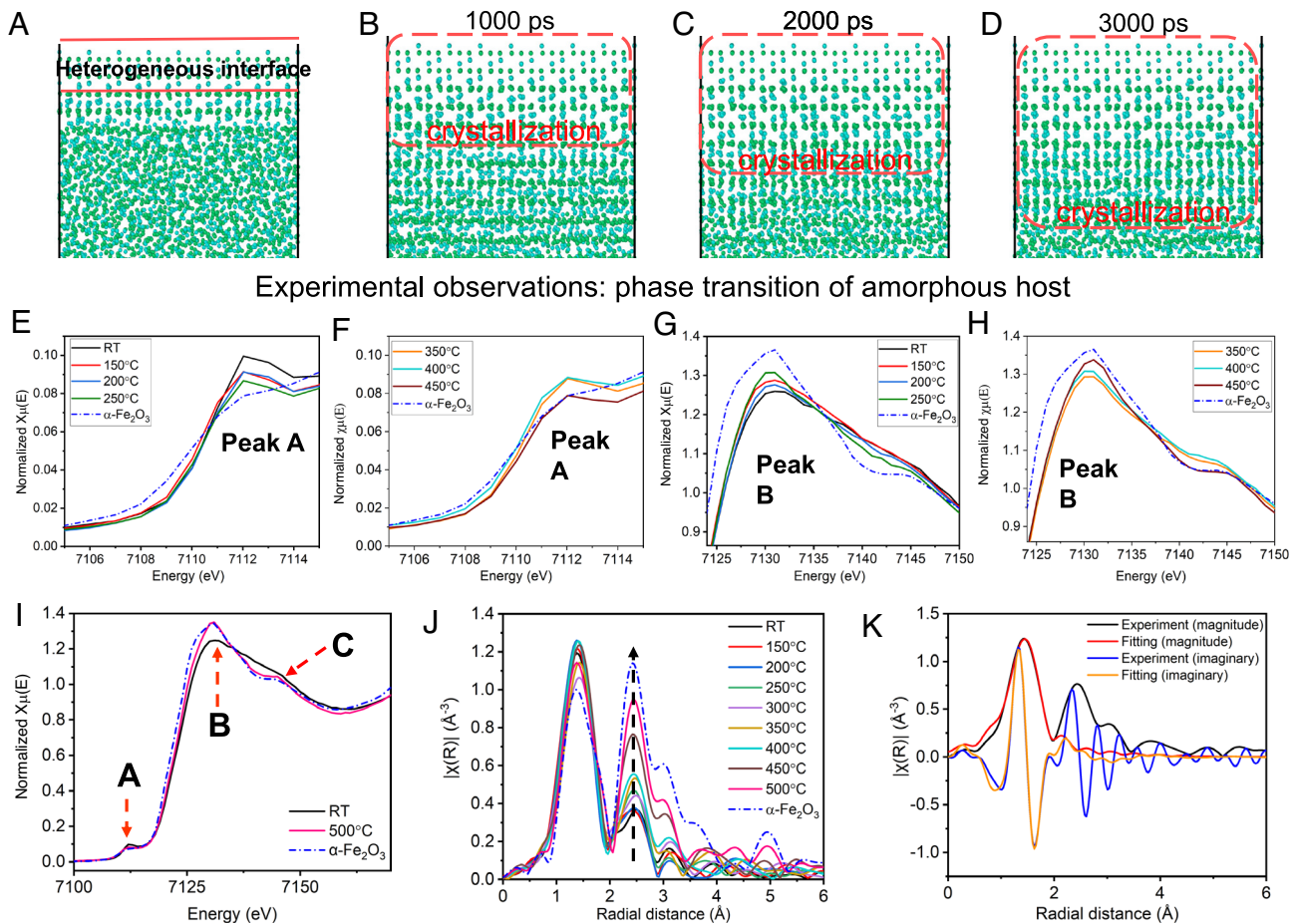


Fig. 3. Phase transition of amorphous host. (A–D) MD simulations of the phase transition of the amorphous host induced by a top atom heterogeneous interface of amorphous Fe_2O_3 : (A) initial amorphous state with a top crystalline heterogeneous interface. (B–D) Crystallization process of amorphous Fe_2O_3 for 3 ns at 800 K. (E–K) X-ray absorption fine structure (XAFS) spectra of the dynamic phase transition process. (E and F) Comparative XANES features for peaks A and B, contrasting as-deposited (RT) devices with those annealed at temperatures ranging from 150 to 250 °C (E) and 350 to 450 °C (F). (G and H) XANES spectra for peak B, juxtaposing the RT and annealed samples within the 150 to 250 °C (G) and 350 to 450 °C (H) intervals. (I) XANES spectral comparison among the RT sample, the one annealed at 500 °C, and the reference $\alpha\text{-Fe}_2\text{O}_3$. (J) K2-weighted Fourier transformed EXAFS analysis comparing the RT device, those annealed from 150 to 500 °C, and the standard $\alpha\text{-Fe}_2\text{O}_3$. (K) First-shell fitting of the non-phase-shift-corrected Fourier transform for the Fe K-edge of the sample annealed at 450 °C, with black and blue indicating experimental results, and red and orange representing calculated results.

heterogeneous nucleation that prompts the phase transition of amorphous Fe_2O_3 downward along the interface. This is in stark contrast to the MD simulations of a uniform amorphous Fe_2O_3 sample annealed under identical conditions, which exhibit no discernible phase transition (*SI Appendix, Fig. S6*). Extended *Movie S3* shows the full annealing process of homogeneous Fe_2O_3 by MD simulations. The heterogeneous interface not only triggers the phase transition but also directs the trajectory of Ag atom movement, enabling reversible atomic manipulation within the material. The intricate modeling and parameters of these MD simulations are detailed in *SI Appendix, Figs. S7–S9*.

To validate the transformation process within the amorphous host, we conducted a comparative experiment utilizing crystalline Fe_2O_3 host layer, highlighting the significant role of the amorphous structure. HRTEM information of the vertically sectioned Ag/c- Fe_2O_3 composite revealed distinct lattice patterns in both materials (refer to *SI Appendix, Fig. S10 A–C*). Postannealing at 300 °C for 1 min, EDX analysis did not show any migration of Ag into the c- Fe_2O_3 layer (*SI Appendix, Fig. S10 D and E*), indicating that noble metal migration is more effective in the amorphous host. Our first-principles MD (ab initio MD, AIMD) simulations align with these experimental observations, showing limited Ag migration into c- Fe_2O_3 under a 600 K (326.85 °C)

thermal environment (detailed in *SI Appendix, Fig. S11*). The presence of a static interface between Ag and the c- Fe_2O_3 layer, as shown in Fig. 2A, impedes Ag movement, thus demonstrating that reversible migration is facilitated uniquely by our heterogeneous interface design in the host structure.

To assess the chemical stability of the host material in proximity to phase transition thresholds, we collected X-ray absorption near edge structure (XANES) spectra at the Fe K-edge from a series of samples subjected to annealing across a temperature spectrum from RT to 500 °C. The corresponding normalized XANES results, along with the benchmark $\alpha\text{-Fe}_2\text{O}_3$, are elaborated in *SI Appendix, Fig. S12*. We have accentuated certain segments of the XANES results, specifically from 7,105 to 7,115 eV in Fig. 3 E and F, and from 7,124 to 7,150 eV in Fig. 3 G and H. Fig. 3 E and G feature the samples annealed from RT up to 250 °C, whereas Fig. 3 F and H present those treated between 350 and 450 °C. Consistently, the edge energy at 7,121 eV, as well as the peak attributes and spectral outlines, are in close agreement with the standard $\alpha\text{-Fe}_2\text{O}_3$, preserving the local symmetry surrounding the Fe^{3+} ions (39). During the annealing process, we observed a rise in the pre-edge peak A, a reduction in peak B, and the development of a distinct shoulder feature around 7,144 eV (feature C) at elevated temperatures. Analysis of the devices at the

annealing extremes (RT and 500 °C, depicted in Fig. 3I) reveals that the spectral characteristics become sharper and more akin to those of standard α -Fe₂O₃ following higher temperature treatments. Generally, X-ray absorption spectra with less pronounced features indicate structural disorder, signifying a long-range order confined to less than three-unit cells (40).

Our investigation extended into the extended X-ray absorption fine structure (EXAFS) spectra, where we conducted numerical analyses to examine changes in the local structure around iron (Fe) postannealing. Fig. 3J displays the Fourier-transformed Fe K-edge EXAFS spectra for devices annealed from RT to 500 °C, alongside standard α -Fe₂O₃. The peak at approximately 1.5 Å correlates with the first coordination shell of Fe–O, and another peak around 2.5 Å corresponds to the second coordination shell of Fe–Fe. The diminished amplitude of the second shell peak in the unannealed sample points to a reduced Fe–Fe coordination number, likely due to significant structural disorder or a high density of vacancies. Notably, annealing at elevated temperatures results in a marked increase in this peak's amplitude, indicative of enhanced long-range order and a transition from amorphous to crystalline phase (41). These findings are corroborated by XRD and SAED results presented in Fig. 2G and *SI Appendix*, Fig. S2.

Nonbinary Solid Metaphotonics for Multilevel Large-Scale Color Tuning. The GRAM concept we've introduced serves as a dynamic method for optical adjustment, enabling the alteration of multilevel optical states and reflective colors in response to the thermal-induced migration of Ag atoms, as illustrated in Fig. 4A. Dual-tuning mechanisms for giant modulation of large-scale structural color are developed via the coherent variation of refractive index and device's structures. The reflection amplitude (r) of a vertical structure with (L) layers is given by the equation: $r = \frac{\eta_m E_m - H_m}{\eta_m E_m + H_m}$ (1), where $\begin{pmatrix} E_m \\ H_m \end{pmatrix} = M \begin{pmatrix} 1 \\ \eta_s \end{pmatrix}$ and E_m and H_m

represent the electric and magnetic vectors, respectively. The matrix (M), which is present in the incident medium, is the cumulative product of matrices given by $M = M_L M_{L-1} \cdots M_j \cdots M_1$.

$M_j = \begin{pmatrix} \cos\delta_j & \frac{i}{\eta_j} \sin\delta_j \\ i\eta_j \sin\delta_j & \cos\delta_j \end{pmatrix}$ (2), where $\delta_j = \frac{2\pi}{\lambda} (n_j d_j \cos\theta_j)$, n_j is the refractive index, d_j is the layer thickness, θ_j is the angle of incidence, and η_j represents the effective refractive index of the medium. The optical behavior, such as the active thin film color of the GRAM device, is predominantly influenced by the dynamic shifts in refractive index and layer thickness due to the movement of Ag.

To investigate this, we constructed a GRAM-based photonic device to examine its tunability with respect to time and temperature. The initial Ag-Fe₂O₃ layer demonstrates rapid and extensive color adjustability across the red, green, and blue spectra when subjected to a thermal field, as evidenced by experimental reflectance spectra and real-time optical microscopy (OM) images (Fig. 4B). Numerical simulations, as shown in Fig. 4B align with the measured spectra from 500 °C to their original states, corroborated by the standard color calibration in CIE 1931 chromaticity diagram (*SI Appendix*, Fig. S14).

The influence of dynamic Ag atoms on color modulation can be methodically evaluated by altering both the thickness (d_j) and refractive index of Fe₂O₃ layer (η_j) under a thermal field. The color simulation depicted in Fig. 4C confirms that the temperature and layer thickness are pivotal in determining the structural colors. *SI Appendix*, Fig. S15 contains the characterization of refractive index of GRAM samples at various temperatures. Direct measurements of the layer thickness in three distinct devices, each with varying Ag atom distributions, demonstrate the correlation between thickness and Ag dispersion [as shown in transmission electron microscopy (TEM)/EDX information and line profiles in *SI Appendix*, Fig. S16]. To showcase the capability for dynamic

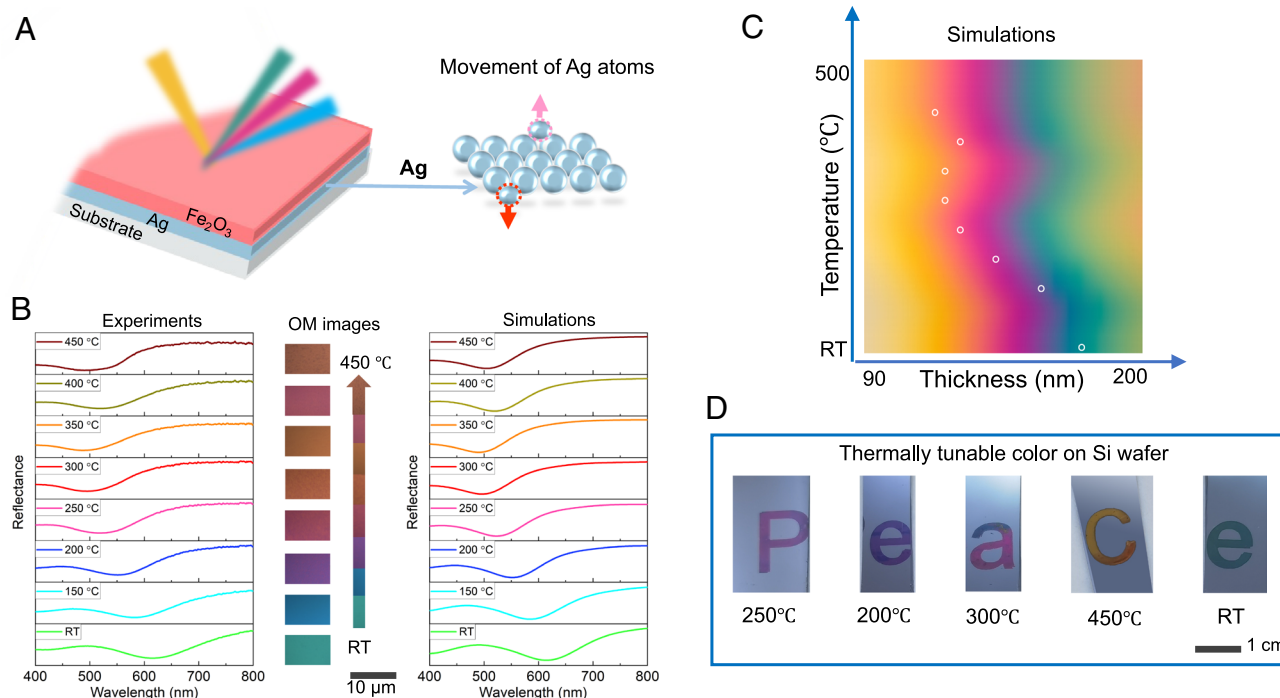


Fig. 4. Proof-of-concept demonstration of nonbinary solid metaphotonics for large-scale color printing. (A) Schematic representation of the adjustable optical instrument utilizing the GRAM concept. (B) On the *Left*, observed reflectance and on the *Right*, computed spectral data for a specimen subjected to various annealing temperatures (ranging from 150 to 450 °C), with OM imagery in natural lighting for each specific temperature. The images include a scale marker of 10 μ m. (C) Color mapping simulations conducted in conjunction with Ag atom adjustments, displaying a gradient of color points from room temperature to 450 °C, arranged from the *Lower Right* to the *Upper Left*. (D) The process of color imprinting and thermally induced color modulation of the word "Peace" on a Si substrate, with photographic evidence of each character exhibiting a spectrum of colors at varying temperatures, denoted by a scale marker of 1 cm.

color creation of any arbitrary image with simple thermal control, we crafted a high-resolution, large-scale colored representation of the word “Peace.” The original and thermally adjusted images at 150 °C are provided in *SI Appendix, Fig. S17*. This multicolor thermal tuning was performed on a roughly $2 \times 5 \text{ cm}^2$ silicon wafer, with each image annealed at distinct temperatures (as seen in Fig. 4D). Notably, the color remains stable even after the thermal field is removed, suggesting that our GRAM design could serve as a large-scale, nonvolatile color display that operates without continuous energy input.

Raster-Scanning Writing Pattern. Our GRAM approach enables the fast generation of large-scale and high-resolution color patterns without the need for complex instrumentation and processes. To demonstrate its potential, we applied our technique to laser raster-scanning pattern (LRSP) generation, which is widely used for semiconductors. We set up a simple home-made laser raster-scanning platform. The one-step laser scanning can generate RGB color patterns on a whole Si wafer (Fig. 5A), and we can in situ observe and adjust the patterns by programming the laser power and scan speed. This is because the laser scanning speed and power affect the behavior of noble metal atoms, and thus produce different color patterns. We printed gradient and reversible color patterns locally by varying the scanning power and speed (Fig. 5B) using a CW laser (wavelength at 532 nm), and gradient color patterns were generated by programming the laser power from 1 to 75 mW with a fixed scanning speed 1 $\mu\text{m}/\text{ms}$. We also demonstrated the reversibility by continuously tuning the laser

scanning power or speed during the LRSP process (Fig. 5C). As a demonstration, we printed a 500×500 pixel image of a Butterfly with individual size of $2 \times 2 \mu\text{m}^2$ (Fig. 5D) in 10 s. The multilevel programmability of the nonbinary metamaterials offers exciting opportunities to incorporate various information into building blocks without specific structures, but with more complex functionalities. Our GRAM approach has shown multilevel information, as noble metal atoms modify the refractive index and structures globally in *SI Appendix, Figs. S15 and S16*. The multilevel information can also be observed in the LRSP process in Fig. 5E, where we printed a typical RGB color flower on the same sample. To demonstrate the reversibility, we used LRSP to draw an image inspired by the artwork (Fig. 5F), *Composition avec bleu, rouge, jaune et noir*, whose color can be reversibly controlled by tuning the laser power. Unlike current reported techniques that use laser to generate colorful patterns, which usually rely on complex nanostructures and specific materials, our technique offers a versatile platform for solid materials without requiring structures for color pattern generation and color tuning techniques from the bottom. The GRAM-based devices remained stable throughout various conditions, according to our experimental data (*SI Appendix, Fig. S18*).

Discussion and Conclusions

In this work, we introduced the GRAM approach, which enables dynamic and reversible modification of optical properties through atomic manipulation. GRAM offers multilevel, nonbinary

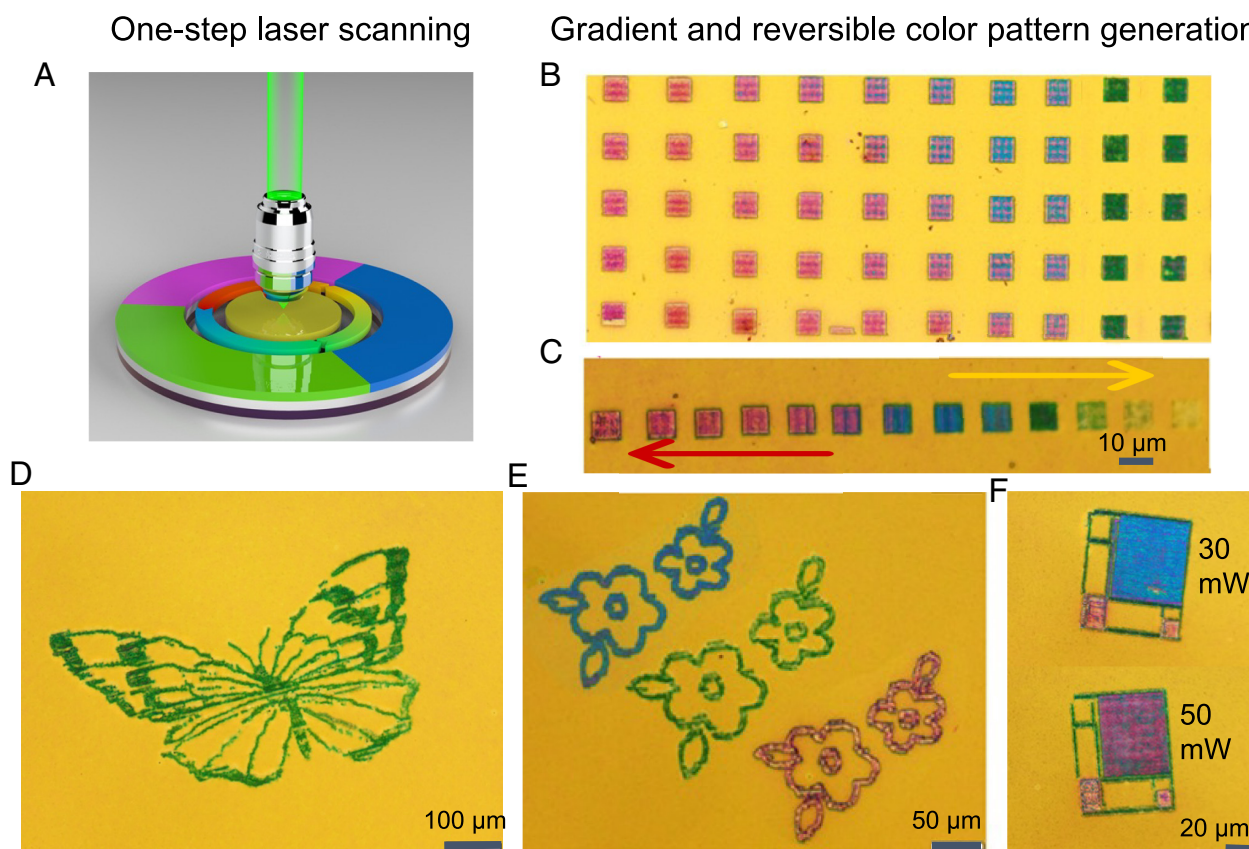


Fig. 5. One-step pattern generation by local laser actuation. (A) Schematic illustration of the gradient and reversible color-pattern generation on a Si wafer using a high-efficiency laser, without complex lithography process. (B) OM images of the raster-scanning pattern with different laser powers from 1 to 75 mW and a fixed speed of 1 $\mu\text{m}/\text{ms}$. (C) OM images of the programmable reversible color pattern with different laser powers from 10 to 75 mW and a fixed speed of 0.3 $\mu\text{m}/\text{ms}$. (D) Large-scale Butterfly demonstration on Si wafer in 10 s with a laser power of 10 mW. (E) RGB color Flower patterns generated by local laser raster-scanning with programmed power. (F) Reversible generation of high-resolution patterns by the GRAM mechanism. The color patterns inspired by *Composition avec bleu, rouge, jaune et noir*.

tunability of material characteristics, significantly broadening its applicability in various photonics applications, such as adaptive optics and information storage. Moreover, it is compatible with conventional semiconductor processing techniques, underscoring its potential for large-scale industrial adoption. However, the GRAM approach requires precise control over atom migration at the picometer scale, raising challenges in terms of technical complexity and associated costs. The dependency on specific noble metals and substantial energy inputs may limit its practical deployment in resource-constrained environments. Nevertheless, GRAM's capability to facilitate precise, programmable modifications at the atomic level positions it as a valuable advancement in enhancing optical material functionalities, striking a compelling balance of innovative capability and practical challenges.

Addressing the scalability and integration of our GRAM technique within existing semiconductor technologies, we identify several challenges that should be carefully managed. Primarily, the technical complexity of scaling the GRAM process presents significant challenges. The need for atomic-scale precision across larger device areas may introduce variability and defects, adversely affecting the uniformity and reliability of the metamaterials' optical properties. Additionally, integrating the GRAM technique into established semiconductor manufacturing lines necessitates adaptations to standard processes, such as implementing precise temperature controls and specialized handling of noble metals, which could complicate production and increase operational costs.

To mitigate these challenges and facilitate the transition of the GRAM technique from a unique concept to a commercially viable technology, several strategies can be employed. A modular design approach would ensure that scalability does not compromise the integrity and functionality of GRAM devices, allowing for the replication and integration of scalable units with high fidelity. Leveraging advanced fabrication techniques, such as atomic layer deposition, could enhance the precision and uniformity of the materials produced. Computational modeling and simulation should also play a crucial role, providing predictive insights and optimization strategies to maintain the tunability and reversibility of the GRAM properties at larger scales. Finally, fostering collaborations with industry stakeholders will ensure that the adaptation of GRAM technologies aligns with existing production capabilities and market needs, addressing practical considerations such as cost-efficiency and throughput requirements. By navigating these challenges with targeted strategies, GRAM can significantly impact the development of advanced optical materials and devices.

In conclusion, we have introduced an innovative method for fabricating tunable nonbinary solid metaphotonic platform by atomic manipulation. By dynamically controlling noble metal atoms within amorphous materials, we achieve reversible, multilevel, and rapid uniform switching. This process is streamlined, avoiding complex manufacturing steps, and is suitable for integration with existing back-end-of-line applications for semiconductor technologies. The key to our approach is the use of a heterogeneous interface, which triggers a phase transition and returns the noble metal atoms to their initial locations. This action permits a controlled and reversible migration of foreign metal atoms, resulting in consistent, multilevel alterations to the composition, refractive index, and structure of metamaterials. Our comprehensive experimental and theoretical investigations have revealed the underlying mechanisms and dynamics of this atomic manipulation. The GRAM mechanism we've developed ensures that the altered state of the material is stable and can be preserved indefinitely without ongoing energy consumption. This represents the first instance of a dynamic interaction between foreign metal atoms and amorphous systems during a phase transition, establishing a standard for the

direct manipulation of various elements within disordered solids and the development of active metaphotonics. We have demonstrated the potential for adjusting large-scale structural colors and creating precise local patterns using laser raster-scanning on a silicon wafer, highlighting the precise control over light–matter interactions. We anticipate that this breakthrough in atomic manipulation will pave the way for discoveries and applications at the picometer scale (42), inspiring further research in the field.

Materials and Methods

Material deposition and device fabrication can be found in Supplementary Note 19.

Microstructure and Materials Characterization. To examine the underlying mechanism, we characterized the microstructure of GRAM samples that were annealed at 200 and 500 °C for 1 min, along with a control sample containing crystalline Fe₂O₃. The cross-sectional specimens were prepared using a dual-beam focused ion beam system, specifically the FEI Helios 600i. For material characterization, we utilized the FEI Tecnai G2 F20 transmission electron microscope in both scanning transmission electron microscopy (STEM) and EDX modes, operating at an accelerating voltage of 200 kV. Bright-field TEM images and selected-area electron diffraction patterns were captured using a JEOL 2100HC, also at 200 kV. Additionally, annular dark-field STEM images and electron energy loss spectra were recorded with a JEOL ARM300CF at 300 kV, with an illumination semiangle of 20 mrad and collection semiangles ranging from 70 to 200 mrad. X-ray absorption near-edge structure spectra at the Fe K-edge and Ag L3-edge were measured at the Singapore Synchrotron Light Source facility. The X-ray absorption spectroscopy data underwent background subtraction, normalization, and Fourier transformation following standard practices, utilizing ATHENA software for processing.

Optical Measurements. We conducted measurements of the reflectance spectra and OM for our samples using a CRAIC 508 PV microspectrophotometer paired with a Nikon Eclipse LV100ND OM setup. The reflectance data were standardized against an enhanced aluminum reference film to ensure accuracy. Images showcasing the Peace pattern, which had undergone annealing at various temperatures, were captured using the rear camera of a Huawei P40 smartphone under a daylight lamp within our laboratory. Additionally, we recorded the color transitions of the thin film under thermal conditions using a Canon EOS RP camera equipped with an RF35mm F1.8 lens, all within a laboratory setting. It is important to note that no color alterations were made during postproduction.

Optical Simulation. We utilized a well-known finite-difference time-domain application (Lumerical, Canada) to simulate the reflectance spectra. The substrate's properties were defined using the software's default data, while the Fe₂O₃ layer was modeled using experimentally obtained refractive indices that vary with temperature. We applied periodic boundary conditions laterally and perfect matching layers vertically to ensure the incident light was absorbed with minimal reflection. A plane wave source was positioned above the structure for even illumination, followed by a monitor to measure the reflectance. We captured the reflectance spectra for various thicknesses of the phase change material (ranging from 90 to 200 nm) at temperatures from room temperature to 500 °C, which were then plotted in the CIE 1931 color space and translated into the sRGB color space for visualization.

MD simulations. MD simulations of Fe₂O₃ were conducted using the Large-scale Atomic/Molecular Massively Parallel Simulator. The atomic interactions were modeled using the Buckingham potential in combination with a Coulomb term,

$$V_{ij}(r_{ij}) = A_{ij} \exp\left(-\frac{r_{ij}}{\rho_{ij}}\right) - \left(\frac{C_{ij}}{r_{ij}^6}\right) + \frac{q_i q_j}{r_{ij}},$$

where the interatomic distance between the atom i and j , represented by r_{ij} with charges q_i and q_j , respectively. The short-range repulsive and attractive interactions are described by the first and second terms with adjustable parameters A_{ij} , ρ_{ij} , and C_{ij} , respectively. The effective distance for pairwise interactions extends up to 8 Å. *SI Appendix, Fig. S14* provides the parameters for each ion. Notably, the Buckingham potential employed in our simulations has been validated to yield a reasonable melting temperature for bulk Fe₂O₃ and has demonstrated success

in modeling the structure evolution of Fe₂O₃ nanoparticles (additional structure information and relevant references are available in *SI Appendix*).

In our experimental configuration, we positioned an α -Fe₂O₃ segment atop a mixed amorphous/crystalline base, spanning 41.06 Å by 35.56 Å in the x and y axes. This base is composed of 512 iron (Fe) atoms and 768 oxygen (O) atoms. During MD simulations, the Fe and O atoms within the substrate's lower stratum, measuring 4 Å in thickness, are immobilized. We apply periodic boundary conditions in every direction and introduce a 20 Å vacuum layer to preclude spurious interactions among periodic replicas. The crystalline portion of the substrate is structured as α -Fe₂O₃ with a (111) surface orientation. To synthesize amorphous α -Fe₂O₃, we initially heat a crystalline array containing 1,536 Fe atoms and 2,304 O atoms to 3,000 K, allowing it to equilibrate for 500 ps in a liquid state under an NPT ensemble. Subsequently, we cool the system to 800 K at a rate of 100 K/ps and maintain it at this temperature for another 500 ps to achieve an amorphous condition. The simulation of α -Fe₂O₃ is conducted under an NPT ensemble, maintaining a steady pressure of 1 atm.

Our MD simulation of the annealing process is conducted within an NVT ensemble framework. We maintain the system at a steady temperature of 800 K using a Nose–Hoover thermostat throughout a 3 ns annealing duration. The integration of motion equations is performed via the velocity-verlet algorithm with a temporal resolution of 1 fs. Snapshot trajectories are recorded at intervals of 1,000 steps. The visualization and analysis of the MD simulation outcomes are facilitated by OVITO software. For further details on our MD modeling, please refer to *SI Appendix, Supplementary Reference*. Information on ab initio molecular dynamics (AIMD) calculations is available in *SI Appendix, Fig. S11*.

Data, Materials, and Software Availability. All study data are included in the article and/or supporting information.

ACKNOWLEDGMENTS. We acknowledge the support from the National Key Research and Development Program of China (No. 2023YFF0613600) and the National Research Foundation, Prime Minister's Office, Singapore, under the Competitive Research Program Award NRF-CRP22-2019-0006. The authors would like to acknowledge the support from the Nanotech Energy and

Environment Platform, National University of Singapore (Suzhou) Research Institute. This work was supported by Science and Technology Project of Jiangsu Province, Grant Number: BZ2022056. J.K.W.Y. acknowledges financial support from the National Research Foundation, Prime Minister's Office, Singapore, under the Competitive Research Program Award NRF-CRP30-2023-0003. This work was supported by the National Natural Science Foundation of China (Nos. 61925504, 62192770). W.W. acknowledges Shandong Provincial Natural Science Foundation (Grant No. ZR2023QA012). We also acknowledge travel funding (SG-ISAP/AS2023/C2-00003) provided by the International Synchrotron Access Program (ISAP) managed by the Australian Synchrotron, part of Australian Nuclear Science and Technology Organisation (ANSTO), and funded by the Australian Government. A.D.H. acknowledges funding from A*STAR through Horizontal Technology Coordinating Offices (HTCO) seed fund (C231218004). We express our gratitude to the senior scientists from Semilab Semiconductor Physics Laboratory, L. Makai and B. Fodor, for their invaluable assistance in measuring the optical index. Additionally, we extend our appreciation to Z.Z., X.B., and Y.H. for their insightful discussions and their contributions to the sample measurement process.

Author affiliations: ^aDepartment of Electrical and Computer Engineering, National University of Singapore, Singapore 117583, Singapore; ^bInstitute of Materials Research and Engineering, Agency for Science, Technology and Research, Singapore 138634, Singapore; ^cKey Laboratory for Liquid-Solid Structural Evolution and Processing of Materials, Ministry of Education, Shandong University, 250061, People's Republic of China; ^dInstitute of Engineering Innovation, The University of Tokyo, Tokyo 113-8656, Japan; ^eDepartment of Engineering Product Design, Singapore University of Technology and Design, Singapore 487372, Singapore; ^fDepartment of Chemistry, University College London, London WC1H 0AJ, United Kingdom; ^gCoastal Engineering Department, Surbana Jurong Consultants Pte Ltd., Singapore 636741, Singapore; ^hZhejiang Lab Nanhui Headquarters, Hangzhou, Zhejiang Province 31500, People's Republic of China; ⁱSchool of Physics Science and Engineering, Tongji University, Shanghai 200092, People's Republic of China; ^jDepartment of Precision Instrument, Center of Brain-Inspired Computing Research, Tsinghua University, Beijing 100084, People's Republic of China; and ^kNanotech Energy and Environment Platform, National University of Singapore Suzhou Research Institute, Suzhou, Jiangsu 215123, People's Republic of China

Author contributions: Z.Y. designed research; Z.Y. and Z.Z. performed research; C.Y., B.F., N.S., R.Z., C.T.C., and Y.I. contributed new reagents/analytic tools; Z.Y., A.D.H., W.W., H.W., M.Y., Z.Z., L.C., X.C., G.W.H., and J.K.W.Y. analyzed data; and Z.Y. and C.-W.Q. wrote the paper.

1. N. I. Zheludev, Y. S. Kivshar, From metamaterials to metadevices. *Nat. Mater.* **11**, 917–924 (2012).
2. Y. Liu, X. Zhang, Metamaterials: A new frontier of science and technology. *Chem. Soc. Rev.* **40**, 2494–2507 (2011).
3. A. Sihvola, Metamaterials in electromagnetics. *Metamaterials* **1**, 2–11 (2007).
4. Y. Liu *et al.*, Dynamic thermal camouflage via a liquid-crystal-based radiative metasurface. *Nanophotonics* **9**, 855–863 (2020).
5. A. Tittl *et al.*, Imaging-based molecular barcoding with pixelated dielectric metasurfaces. *Science* **360**, 1105–1109 (2018).
6. A. M. Shaltout, V. M. Shalae, M. L. Brongersma, Spatiotemporal light control with active metasurfaces. *Science* **364**, eaat3100 (2019).
7. T. Gu, H. J. Kim, C. Rivero-Baleine, J. Hu, Reconfigurable metasurfaces towards commercial success. *Nat. Photonics* **17**, 48–58 (2023).
8. M. Song *et al.*, Versatile full-color nanopainting enabled by a pixelated plasmonic metasurface. *Nat. Nanotechnol.* **18**, 71–78 (2023).
9. M. Y. Shalaginov *et al.*, Reconfigurable all-dielectric metalens with diffraction-limited performance. *Nat. Commun.* **12**, 1225 (2021).
10. J. Park *et al.*, All-solid-state spatial light modulator with independent phase and amplitude control for three-dimensional LiDAR applications. *Nat. Nanotechnol.* **16**, 69–76 (2021).
11. D. Fattal *et al.*, A multi-directional backlight for a wide-angle, glasses-free three-dimensional display. *Nature* **495**, 348–351 (2013).
12. W.-J. Joo *et al.*, Metasurface-driven OLED displays beyond 10,000 pixels per inch. *Science* **370**, 459–463 (2020).
13. T. An *et al.*, Strain to shine: Stretching-induced three-dimensional symmetries in nanoparticle-assembled photonic crystals. *Nat. Commun.* **15**, 5215 (2024).
14. R. R. Sahu *et al.*, Single-step fabrication of liquid gallium nanoparticles via capillary interaction for dynamic structural colors. *Nat. Nanotechnol.* **19**, 766–774 (2024).
15. S.-U. Kim *et al.*, Broadband and pixelated camouflage in inflating chiral nematic liquid crystalline elastomers. *Nat. Mater.* **21**, 41–46 (2022).
16. B. H. Miller, H. Liu, M. Kollé, Scalable optical manufacture of dynamic structural color in stretchable materials. *Nat. Mater.* **21**, 1014–1018 (2022).
17. M. Zhang *et al.*, Hydrogel muscles powering reconfigurable micro-metastuctures with wide-spectrum programmability. *Nat. Mater.* **22**, 1243–1252 (2023).
18. Q. Wang *et al.*, Optically reconfigurable metasurfaces and photonic devices based on phase change materials. *Nat. Photonics* **10**, 60–65 (2016).
19. Y. Zhang *et al.*, Electrically reconfigurable non-volatile metasurface using low-loss optical phase-change material. *Nat. Nanotechnol.* **16**, 661–666 (2021).
20. P. Hosseini, C. D. Wright, H. Bhaskaran, An optoelectronic framework enabled by low-dimensional phase-change films. *Nature* **511**, 206–211 (2014).
21. C. Jung *et al.*, Metasurface-driven optically variable devices. *Chem. Rev.* **121**, 13013–13050 (2021).
22. X. Duan, S. Kamin, N. Liu, Dynamic plasmonic color display. *Nat. Commun.* **8**, 14606 (2017).
23. X. Zhu, C. Vannahme, E. Højlund-Nielsen, N. A. Mortensen, A. Kristensen, Plasmonic color laser printing. *Nat. Nanotechnol.* **11**, 325–329 (2016).
24. R. Feynman, *Feynman Lectures on Gravitation* (CRC Press, 2018).
25. O. Custance, R. Perez, S. Morita, Atomic force microscopy as a tool for atom manipulation. *Nat. Nanotechnol.* **4**, 803–810 (2009).
26. X. Zhou *et al.*, A single-atom manipulation approach for synthesis of atomically mixed nanoalloys as efficient catalysts. *Angew. Chem. Int. Ed. Engl.* **132**, 13670–13676 (2020).
27. D. G. Grier, A revolution in optical manipulation. *Nature* **424**, 810–816 (2003).
28. Y. Sugimoto *et al.*, Complex patterning by vertical interchange atom manipulation using atomic force microscopy. *Science* **322**, 413–417 (2008).
29. U. Celano *et al.*, Three-dimensional observation of the conductive filament in nanoscaled resistive memory devices. *Nano. Lett.* **14**, 2401–2406 (2014).
30. G. W. Burr *et al.*, Neuromorphic computing using non-volatile memory. *Adv. Phys. X* **2**, 89–124 (2017).
31. K. Wang *et al.*, Electrical control of charged carriers and excitons in atomically thin materials. *Nat. Nanotechnol.* **13**, 128–132 (2018).
32. Z. Yan *et al.*, Floating solid-state thin films with dynamic structural color. *Nat. Nanotechnol.* **16**, 795–801 (2021).
33. R. A. Street, Doping and the Fermi energy in amorphous silicon. *Phys. Rev. Lett.* **49**, 1187 (1982).
34. S. Jeong, Y. G. Ha, J. Moon, A. Facchetti, T. J. Marks, Role of gallium doping in dramatically lowering amorphous-oxide processing temperatures for solution-derived indium zinc oxide thin-film transistors. *Adv. Mater.* **22**, 1346–1350 (2010).
35. K. Nomura *et al.*, Room-temperature fabrication of transparent flexible thin-film transistors using amorphous oxide semiconductors. *Nature* **432**, 488–492 (2004).
36. Z. Wang *et al.*, Resistive switching materials for information processing. *Nat. Rev. Mater.* **5**, 173–195 (2020).
37. H. Yeon *et al.*, Alloying conducting channels for reliable neuromorphic computing. *Nat. Nanotechnol.* **15**, 574–579 (2020).
38. C. Li *et al.*, High-performance quasi-solid-state flexible aqueous rechargeable Ag-Zn battery based on metal-organic framework-derived Ag nanowires. *ACS Energy Lett.* **3**, 2761–2768 (2018).
39. D. Larcher *et al.*, Combined XRD, EXAFS, and Mössbauer Studies of the reduction by lithium of α -Fe₂O₃ with various particle sizes. *J. Electrochem. Soc.* **150**, A1643 (2003).
40. Y. Zhang, O. Ersoy, A. Karatutlu, A. Sapelkin, Local structure of amorphous and nanoscale systems by numerical XANES calculations. *J. Non-Cry. Solids* **451**, 10–15 (2016).
41. A. Moreira, F. Paula, A. Campos, J. Depeyrot, Local structure investigation of cobalt ferrite-based nanoparticles by synchrotron X-ray diffraction and absorption spectroscopy. *J. Solid State Chem.* **286**, 121269 (2020).
42. T. Liu *et al.*, Picophotonic localization metrology beyond thermal fluctuations. *Nat. Mater.* **22**, 844–847 (2023).